IEEE Journal of Microwaves

Received 21 July 2021; revised 26 August 2021; accepted 8 September 2021. Date of publication 29 September 2021; date of current version 7 October 2021.

Digital Object Identifier 10.1109/JMW.2021.3111965

Local Dosimetry at Cellular and Subcellular Level in HF and Millimeter-Wave Bands

ZAIN HAIDER [1], DENYS NIKOLAYEV [1] (Member, IEEE), YVES LE DRÉAN [2], ANNALISA DE ANGELIS [3,4] (Member, IEEE), MICAELA LIBERTI [3,4] (Member, IEEE), RONAN SAULEAU [1] (Fellow, IEEE), AND MAXIM ZHADOBOV [1] (Senior Member, IEEE)

[1]CNRS, Institut d'Électronique et des Technologies du numéRique (IETR), UMR 6164, Univ Rennes, F-35000 Rennes, France
[2]Inserm, EHESP, Institut de Recherche en Santé, Environnement et Travail (IRSET) - UMR_S 1085, F-35000 Rennes, France
[3]Department of Information Engineering, Electronics and Telecommunications (DIET), Sapienza University of Rome, 00185 Rome, Italy
[4]Center for Life Nano Science@Sapienza, Istituto Italiano di Tecnologia, 00185 Rome, Italy

CORRESPONDING AUTHOR: Zain Haider (e-mail: zain.haider@univ-rennes1.fr).

This work was supported in part by the French National Research Program for Environmental and Occupational Health of ANSES under Grant 2018/2 RF/07 through the NEAR 5G Project; in part by the French government support granted to the CominLabs excellence laboratory and managed by the National Research Agency in the "Investing for the Future" program under Grant ANR-10-LABX-07-01; in part by the European Union through the European Regional Development Fund (ERDF); and in part by the French Region of Brittany, Ministry of Higher Education and Research, Rennes Métropole and Conseil Départemental 35, through the CPER Project SOPHIE / STIC & Ondes.

ABSTRACT The aim of this study was to investigate quantitatively local sub-cellular power deposition at frequencies upcoming for wireless power transfer (WPT) and millimeter-wave (mmWave) technologies. The study was performed on a realistic two-dimensional keratinocyte cell model, designed based on electron microscopy images and experimental data on surface area fraction of keratinocyte to explicitly represent nucleus, mitochondria, endoplasmic reticulum, Golgi apparatus and vesicles. The average power loss density ($\boldsymbol{PLD}_{\mathrm{avg}}$) and electric field ($\boldsymbol{E}_{\mathrm{avg}}$) were computed by solving Laplace's equation under quasi-static approximation using the finite element method. The numerical results for the spherical cell model were validated with corresponding analytical solutions. The results showed that $\boldsymbol{E}_{\mathrm{avg}}$ and $\boldsymbol{PLD}_{\mathrm{avg}}$ inside the organelles increased with frequency. Nearly, 51.8% and 98.9% of the incident field on the cell penetrated inside the organelles at 6.78 MHz and 60 GHz, respectively. The $\boldsymbol{PLD}_{\mathrm{avg}}$ within the organelles in average was 35.7% (6.78 MHz) and 1.95% (60 GHz) lower than in the cytoplasm. The $\boldsymbol{E}_{\mathrm{avg}}$ induced inside nuclear pores ($\mathrm{N_p}$) exceeded the incident field by 5 times and 1.1 times at 6.78 MHz and 60 GHz, respectively. The corresponding $\boldsymbol{PLD}_{\mathrm{avg}}$ within $\mathrm{N_p}$ was 32.7 times (6.78 MHz) and 1.2 times (60 GHz) higher than that of the cytoplasm. The enhancement of $\boldsymbol{PLD}_{\mathrm{avg}}$ in $\mathrm{N_p}$ suggests that the intracellular traffic is locally exposed to higher exposure levels compared to the background $\boldsymbol{PLD}_{\mathrm{avg}}$ in cytosol.

INDEX TERMS Dosimetry, finite element method, human skin, millimeter waves.

I. INTRODUCTION

Over the past few years, the demand for global mobile data traffic has been skyrocketing. The latest Visual Network Index (VNI) report from Cisco has forecasted a seven-fold increase in worldwide mobile data traffic between 2017 and 2022, reaching 77 exabytes per month by 2022 [1]. This avalanche of mobile data traffic is mainly driven by proliferation of massive number of wireless-connected devices. In addition, the emerging Internet of Things (IoT) devices are expected to reach 80 billion by 2030 [2]. These unprecedented developments have led to spectral crunch over traditional microwave communication frequency bands. Amidst this data revolution, the underutilized millimeter wave (mmWave) spectrum is the frontier for next generation commercial wireless communication systems due to its potential to offer wide bandwidth resources spanning from 30 to 300 GHz [3]–[6]. The paradigm shift towards mmWave technologies is also ascribable to ultra-low latency (<1 ms), superior data rates (multi-Gbps), secure communications, and compact size of devices [7].

The aforementioned vision of wirelessly connecting billions of IoT devices is constrained by the impracticality of

periodically recharging or replacing the batteries for energy supply. The inductive power transfer (IPT) based on magnetic coupling (near-field) is a promising solution for energizing electronic devices over short distances [8]. Wireless power transfer (WPT) technologies have seen an upsurge of interest due to user friendliness, operational flexibility, cost effectiveness, and capability to provide stable, and perpetual energy source. The expeditious exploration of mmWave and WPT technologies has prompted concern and uncertainty among general public and scientific community regarding potential biological and health effects.

Experimental techniques utilized to measure the distribution of the electrical potential at the cellular level are essentially limited to potentiometric fluorescent dyes [9]. Therefore, analytical, circuital and numerical methods are employed frequently to evaluate the electric field ($\boldsymbol{E}$) distribution at the microscopic level. Analytical studies on simplified models provide an intuitive groundwork for developing and analyzing more realistic cell models [10]–[13]. The biological cells have also been modeled in terms of circuit elements [14]. However, the circuit models cannot be used to investigate spatial variation of the internal $\boldsymbol{E}$.

The significance of the realistic cell anatomies in determining the microscopic $\boldsymbol{E}$ distribution can be accurately quantified by numerical methods. Specifically, the numerical studies based on distributed network method (DNM) [15], meshed transport network method (MTNM) [16], [17], and finite element method (FEM) [18] have been reported. The MTNM and DNM employ equivalent distributed circuits to represent spatial variation of various cellular compartments. Moreover, FEM has been extensively employed to compute the transmembrane potential (TMP) of 2D neurons [18], three dimensional (3D) Chinese hamster ovary cell [19], 3D erythrocyte [20], super formula based 3D keratinocytes [21], 2D nucleus [22], 2D [23], and 3D [24] endoplasmic reticulum (ER) and axisymmetric model of isolated mitochondria [25]. Additionally, the numerical investigations performed in [18] and [20] employed dispersive electromagnetic cell model. Furthermore, numerical and experimental studies performed in the context of electroporation have established the capability of high frequency spectral content of nano- or picosecond pulses to penetrate the plasma membrane (P_m) and reach the organelle interior [26], [27]. To the best of authors' knowledge, most microdosimetry studies to date have been performed up to microwave frequencies with the primary focus at evaluating the TMP.

In this paper, a realistic geometry of a 2D keratinocyte is presented that explicitly incorporates the geometric details and concentrations of various cellular organelles (nucleus, mitochondria, ER, Golgi apparatus (GA), vesicles). The aim of this microdosimetric study is to gain a quantitative insight into the role of organelle density, position, size, and orientation on the $\boldsymbol{E}$ field and power deposition inside a generic keratinocyte cell model at frequencies upcoming for next-generation wireless communications (60 GHz) and power transfer (6.78 MHz).

TABLE 1. List of Cellular Component Acronyms

Symbol	Definition	Symbol	Definition
P_m	Plasma membrane	N_i	Nucleus
N_m	Nuclear membrane	N_p	Nuclear pores
ER_m	Endoplasmic reticulum membrane	ER_L	Endoplasmic reticulum lumen
GA_m	Golgi apparatus membrane	GA_L	Golgi apparatus lumen
M_{om}	Mitochondria outer membrane	M_{ims}	Mitochondria intermembrane space
M_{im}	Mitochondria inner membrane	N_{ims}	Nucleus intermembrane space
V_m	Vesicle membrane	M_L	Mitochondria lumen
CP	Cytoplasm	V_L	Vesicle lumen
EXM	Extracellular medium	SC_m	Subcellular membranes

The rest of the paper is organized as follows: Section II A presents the geometric features of the 2D cell, followed by a description of the electromagnetic model of the cell in Section II B. The numerical approach adopted to perform microdosimetric analysis is reported in Section II C. Finally, the results and conclusions are included in Section III and IV.

II. MATERIALS AND METHODS

A. CELL MODEL

As at mmWaves the penetration depth is mainly limited to skin, we used keratinocytes as a representative skin cell. Table 1 lists the cellular component acronyms used in the paper.

1) GEOMETRY OF A GENERIC SKIN CELL AND ORGANELLES

A typical basal keratinocyte is represented by a ≈14 μm length structure [28] and was designed based on an electron microscopy image (Fig. 1) [29]. The cell is surrounded by a 5-nm-thick plasma membrane (P_m) [26]. The P_m also has several villous foldings that are used to interlock with adjacent cells. The organelle volume fraction data were obtained from measurements performed on basal keratinocytes in [30] and were converted to 2D surface area fractions by using spherical approximation.

NUCLEUS.

The basal keratinocyte's nucleus (N_i) has a nearly elliptical structure with a major and minor radius of 3.5 μm and 2.1–75 μm, respectively. It constitutes 26.3% of 2D cross section of a typical cell (referred in the rest of the paper as the cell surface area) (volume fraction = 25.9%). This is a typical surface area extracted from measurements performed on submammary and iliac crest region epidermis [30]. The typical radius of nucleolus is 0.6 μm. The nucleus is surrounded by two 5 nm-thick lipid bilayers forming the nuclear membrane (N_m) with an intermembrane space (N_{ims}) of 60 nm as displayed in Fig. 1(c) [31]. In addition, nine nuclear pores (N_p) with a thickness of 9 nm each have been modeled [32], [33].

GOLGI APPARATUS.

On one side of the nucleus, five stacked layers of oval membrane (GA_m) bound compartments surrounded by several

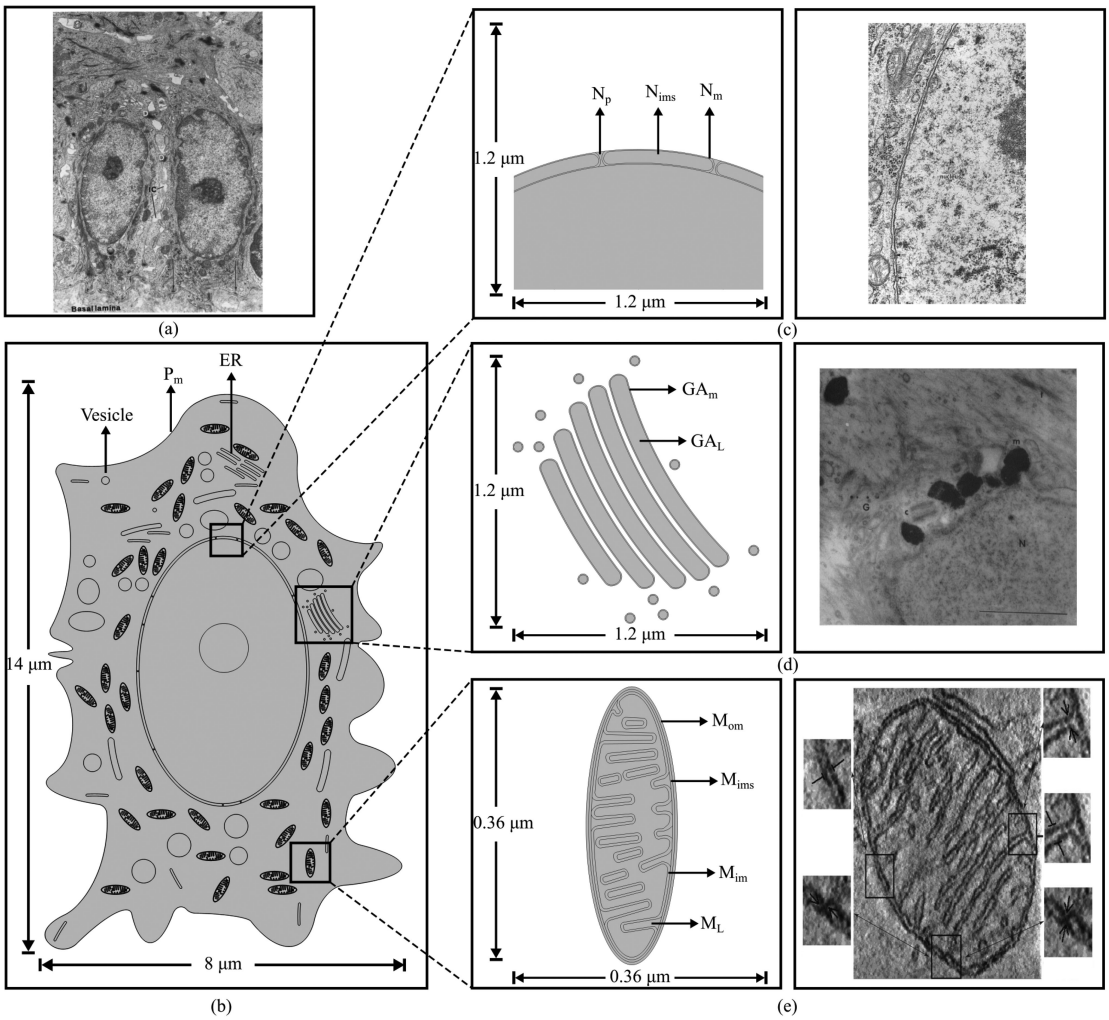

FIGURE 1. Geometric model: (a) basal keratinocyte electron microscopy image [29]; (b) 2D model of Basal keratinocyte; (c) nucleus electron microscopy image [37] and 2D model; (d) GA electron microscopy image [31] and 2D model; (e) mitochondria electron microscopy image [36] and 2D model. Reprinted with the permissions from Elsevier.

50 nm round vesicles form the GA (Fig. 1(d)). The cisternal luminal space (GA_L) is roughly 90 nm thick [31] and the length of cisternae is 0.5–1 µm [34]. The inter-cisternae separation has a typical value of 20 nm [35]. The GA comprises 0.5% of cell surface area in basal keratinocytes (volume fraction = 0.065%).

MITOCHONDRIA.

The mitochondrion is represented by an ellipse with average radii of major and minor axis of 0.365 µm (0.125–0.5 µm) and 0.12 µm (0.075–0.125 µm), respectively [31]. It is based on the electron microscopy image displayed in Fig. 1(e) [36]. The mitochondria lumen (M_L) is bounded by two 7-nm-thick membranes separated by roughly 6-nm-wide gap known as mitochondria intermembrane space (M_{ims}) [37]. The inner mitochondria membrane (M_{im}) is folded extensively to form invaginations called cristae, with a typical width of 27 nm and a length up to several hundred nanometers. The mitochondria occupy about 4.6% of cell surface area (volume fraction = 1.9%).

ENDOPLASMIC RETICULUM.

The ER is comprised of a network of flattened sacs known as cisternae, bounded by a membrane (ER_m) identical to P_m. The cisternal space (ER_L) is typically 50-150 nm wide and saccules are about 0.4–1 µm long [38]. In keratinocytes, the ER tubules constitute roughly 1.5% of cell surface area (volume fraction = 0.35%) and are randomly distributed in cytoplasm (CP) as shown in Fig. 1(b). Keratinocytes have the particularity of having a poorly developed ER, undoubtedly in relation to their physiological role of barrier which does not require a significant secretion of proteins in absence of injury [30], [39].

OTHER ORGANELLES.

The circles and ellipses with 50-900-nm diameter represent lysosomes, secretory vesicles, membrane coating granules and melanosomes. Their lumen (V_L) is limited by a 5-nm-thick lipid bilayer membrane (V_m) and are distributed randomly throughout the CP constituting about 3.6% of the cell surface area (volume fraction = 0.87%).

Note that basal keratinocytes exhibit enormous diversity in size even among the cells with similar genetic composition

TABLE 2. Debye Model Parameters for Different Cellular Compartments

Compartment	ε_s	ε_∞	f_{relax}	σ_{dc} (S/m)
P_m [20]	12.27	1.92	325.60 MHz	10^{-7}
SC_m [40]	11.7	4	179.85 MHz	1.1×10^{-7}
M_{om} [25], [40]	11.7	4	179.85 MHz	1×10^{-4}
EXM [41]	76	6.9	18.5 GHz	1
CP [40], [43]	67	5	17.9 GHz	0.32
Organelle lumen [40]	67	5	17.9 GHz	0.55

and external conditions [28]. The selected dimensions agree with previously reported data on typical dimensions of keratinocyte organelles [31].

B. ELECTROMAGNETIC PROPERTIES

The dispersive electromagnetic properties of cellular compartments and membranes can be described by Debye model

$$\varepsilon^*(f) = \frac{\sigma_{dc}}{j\varepsilon_0 2\pi f} + \frac{\varepsilon_s - \varepsilon_\infty}{1 + jf/f_{\text{relax}}} + \varepsilon_\infty \tag{1}$$

where σ_{dc} is the static conductivity, ε_0 the permittivity of free space, ε_s the static permittivity, ε_∞ the permittivity at high frequencies, and f_{relax} the relaxation frequency. These parameters, reported in the literature for different cellular compartments, are summarized in Table 2.

1) CELLULAR COMPARTMENTS

CP, extracellular medium (EXM), and organelle interior were modeled as electrolytes in free water with dielectric parameters of phosphate buffer saline (PBS) measured at 26 °C and 27 °C respectively in [40], [41] (Table 2). This is confirmed by [42] as saline solution is the main constituent of intracellular and intercellular fluids. Additionally, the CP model was further refined by assignment of static conductivity ($\sigma_{dc} = 0.32$ S/m) based on measurements performed on CP of Jurkat cells [43]. Lastly, the dielectric properties of N_p were also assumed to be that of saline solution as N_p contains aqueous passages freely permeable to small water-soluble molecules (less than 30 kDa) [44], [45].

2) MEMBRANE

The Debye parameters of the P_m were acquired through theoretical and experimental methodology elaborated in [20], which is based on permittivity (ε) measurements of erythrocyte suspensions and inverse application of mixture equation. This electromagnetic model also takes into account effects of channel proteins. On the other hand, the Debye parameters of subcellular membranes (SC_m) are considered equal to that of pure phospholipid membrane, which were attained in [40] by fitting measured permittivity of liposome solutions using mixture equations. The major components of SC_m are phospholipid molecules and are likely to exhibit the same polarization mechanism in terms of dipole orientation and Maxwell-Wagner polarization. Note that porous nature of M_{om} leads to a higher static conductivity [25]. The aforementioned continuum dielectric approximation for two molecule thick membrane is widely accepted in literature [10], [13], [20] as in ordinary matter there are still $\approx 10^6$ nuclei and electrons in 10^{-24} m^3 volume [46].

C. NUMERICAL MODEL

We used the FEM implemented in COMSOL Multiphysics. The analysis was performed over 1-kHz-100-GHz range with special focus on 6.78 MHz and 60 GHz. Quasi-static approximation was applied as the cell dimensions are much smaller than the wavelength (e.g., at 60 GHz, the cell size is roughly 0.0034λ). Electrodes were modeled as electric potential (Dirichlet boundary condition) assigned to the upper and lower edges of the computational domain. The upper electrode at $y = 20$ μm was set to 40 μV, and the lower one at $y = -20$ μm to ground. The potential was chosen to induce a uniform cell exposure at $|E| = 1$ V/m. Note that the current basic restrictions for electromagnetic field exposure recommended by the International Commission on Non-Ionizing Radiation Protection (ICNIRP) [47] correspond to $|E| = 61.8$ V/m (60 GHz) and $|E| = 915.3$ V/m (6.78 MHz) at the skin surface. The $|E|$ at the skin surface was evaluated using a homogeneous skin model (1 mm) at 60 GHz [48]. The electric insulation conditions were applied to the remaining boundaries ascertaining that no electric current flows into these boundaries.

The 2D approximation was used since extremely dense local mesh is required to model ≈5-nm-thick membranes and a 3D model would result in unpractical memory requirements and simulation time. Such simplified 2D models have been employed in microdosimetric [18] and electroporation studies [16], [17], [49]. The smallest mesh cell size in the membranes was 0.5 nm. For the remaining domains, maximum mesh cell size was kept at 400 nm that resulted in 27866908 mesh elements (tetrahedral Lagrange quadratic) and 55734217 degrees of freedom. The dimensions of the computational domain were fine tuned to perform simulations within a reasonable computational time. The Laplace equation was used to calculate electric potential distribution in the cell and organelles:

$$-\nabla \cdot (\sigma + j\omega\varepsilon_0\varepsilon_r')\nabla V = 0 \tag{2}$$

where $\sigma = \omega\varepsilon_0\varepsilon_r''$ is the total conductivity ε_r' and ε_r'' are the real and imaginary parts of complex relative permittivity respectively. Lastly, $\boldsymbol{E}$ distribution was computed from the induced electric potential distribution in the cell and organelles ($E = -\nabla V$). The numerical method used in this work was previously validated in various studies [18]–[21], [24]–[26].

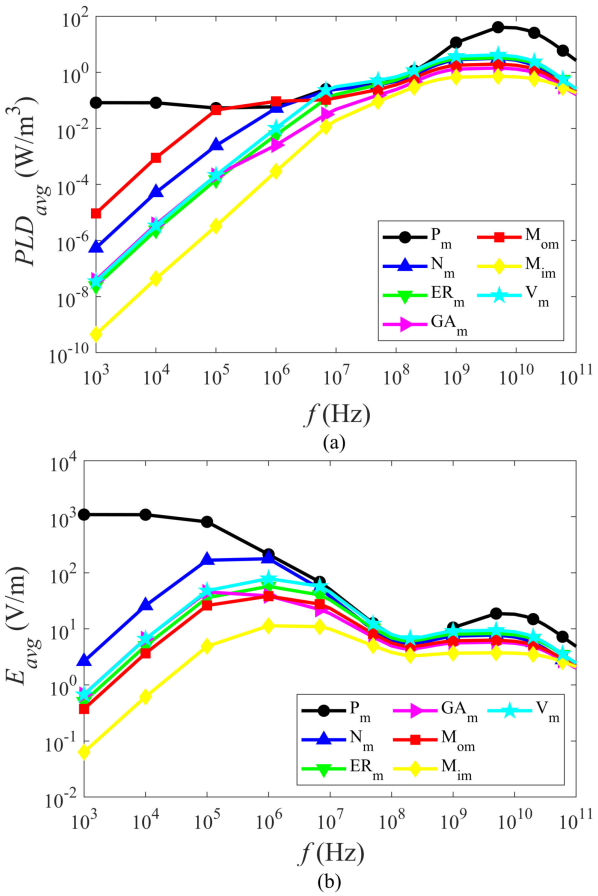

FIGURE 2. Dispersive trend inside membranes: (a) PLD_{avg}; (b) E_{avg}.

D. DOSIMETRY METRICS

The two primary local dosimetry metrics considered by ICNIRP are the following: (1) specific absorption rate (SAR) averaged over a 10-g cubic volume below 6 GHz; and (2) absorbed power density (APD) averaged over 2 cm × 2 cm area above 6 GHz [47]. However, the mass (≈pg) and the size of a cell (≈μm) are much smaller than the averaging mass and averaging surface area considered in the ICNIRP guidelines. As both SAR and APD are derivatives of the absorbed power, we used the local power loss ($\sigma \boldsymbol{E}^2$) as a metric, which quantifies the absorbed power per unit volume. Note that the power loss is directly proportional to SAR as well as to APD and it is used as a source of heating in the heat transfer equation [50].

III. RESULTS

First, the dispersive behavior of the keratinocyte cell model is studied. Afterwards, the role of size, position, and orientation of the organelles on the distribution of the power loss and $\boldsymbol{E}$ are investigated.

TABLE 3. Power Absorption in Membranes

Membranes	$PLD_{avg}(W/m^3)$ 6.78 MHz	$PLD_{avg}(W/m^3)$ 60 GHz
P_m	0.25	5.93
N_m	0.22	0.38
ER_m	0.11	0.55
GA_m	0.031	0.31
M_{om}	0.11	0.39
M_{im}	0.011	0.29
V_m	0.23	0.56

A. FREQUENCY DEPENDENT RESPONSE

1) MEMBRANES

Fig. 2(a) shows the frequency dependence (1 kHz–100 GHz range) of the averaged over the organelle volume power loss (PLD_{avg}) in P $_m$ and SC$_m$. Despite the low effective conductivity (which accounts for the static conductivity and dielectric relaxation; for the sake of brevity the effective conductivity is referred as conductivity in the rest of the paper) (≈10^{-7} S/m) at 1 kHz, the power loss in P$_m$ is 82.6 mW/m^3. This power absorption is due to the migration and accumulation of electric charges towards the insulating P$_m$, which develop a strong reaction $\boldsymbol{E}$ more intense ($E_{avg} = 1.09$ kV/m) and opposite to the applied $\boldsymbol{E}$ (Fig. 2(b)). The conductivity of the medium around the P$_m$ determines the resistance to this mechanism of charge redistribution. This feature shields the cell interior at 1 kHz (i.e., the power loss in all SC$_m$ is below 9.3 μ W/m^3). Note that the power loss inside M$_{im}$ is four orders of magnitude lower than that in M$_{om}$ due to additional shielding provided by the latter.

The power loss in SC$_m$ increases swiftly in the frequency range between 1 kHz and 1 MHz as shown in Fig. 2(a). This increase is due to the rise in the conductivity of P$_m$, which in turn results in a higher penetration of $\boldsymbol{E}$ inside the cell (Fig. 2(b)). At 6.78 MHz, the power loss in cellular and subcellular membranes is tabulated in Table 3.

Note that the E_{avg} in all membranes decreases above 6.78 MHz and reaches a local minimum around 100 MHz. Contrarily, in spite of the decrease of the E_{avg} above 6.78 MHz, the monotonic increase of the power loss in P$_m$ and SC$_m$ is due to the rise of their conductivity in the MHz range where the restricted rotational mobility of the lipid head-groups causes the P$_m$ and SC$_m$ dielectric relaxation.

Above 100 MHz, the power loss in P$_m$ and SC$_m$ continues to rise steadily as depicted in Fig. 2(a). The local peak in all membranes occurs roughly at 5 GHz and the highest absorption is in P$_m$ (40.6 W/m^3). Above 5 GHz, the power loss in P$_m$ and SC$_m$ begins to decrease due to the decrease of $\boldsymbol{E}$ in membranes. The reduction of $\boldsymbol{E}$ in membranes is due to the relaxation of free water in CP, organelle interior, and EXM. In other words, the rise in conductivity of cellular compartments and EXM leads to lower $\boldsymbol{E}$ incident on P$_m$ and

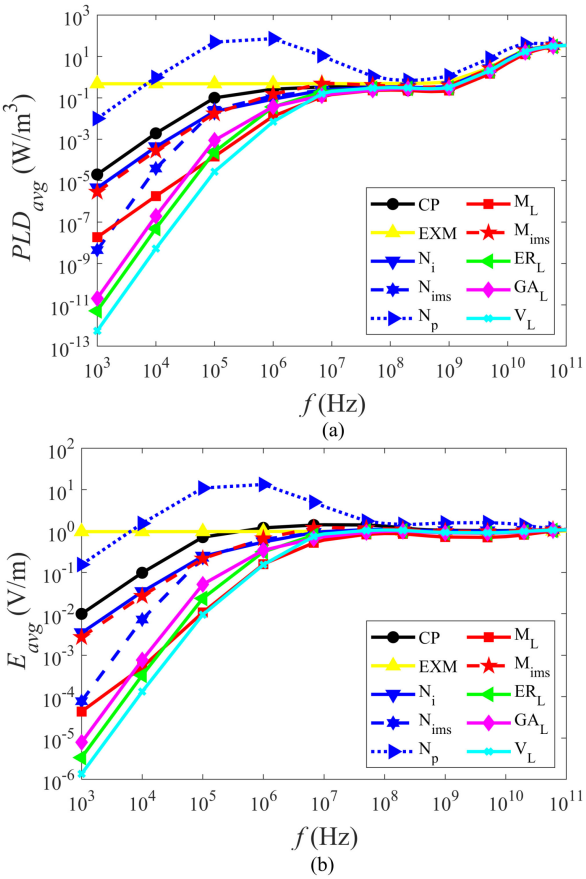

FIGURE 3. Dispersive trend inside cellular organelles: (a) PLD_{avg}; (b) E_{avg}.

SC_m. At 60 GHz, the lower power loss in M_{im} in comparison to M_{om} is due to the insulating nature of the latter.

2) CELLULAR COMPARTMENTS

At 1 kHz, the power loss inside all organelles is less than 19.8 μW/m^3 mainly due to the shielding effect of the membranes (Fig. 3(a)). The power loss in CP and intracellular organelles increases in the frequency range from 1 kHz to 10 MHz. The rise in power loss is because of the diminished shielding effect of the P_m, which in turn results in the penetration of $\boldsymbol{E}$ inside the cell.

At 6.78 MHz, the power loss in various cellular compartments is reported in Table 4. Note that the power loss in M_{ims} is higher than in the rest of the cellular compartments due to higher induced $\boldsymbol{E}$, which results from local distortion of $\boldsymbol{E}$ near M_{om} and M_{im} within CP. In addition, the power loss in EXM is higher than in the CP due to its higher conductivity. Note that below 100 MHz, the ionic conductivity predominantly determines the losses, which is controlled by the size and concentration of ions [51]. The alternating conduction currents are produced by oscillatory motion of ions that are restricted by the frictional forces and cause losses.

The power loss in N_p is higher between 10 kHz and 10 MHz as shown in Fig. 3(a). The maximum power loss in N_p is 72.03 W/m^3 at 1 MHz. The higher E_{avg} (13.3 V/m) is because

TABLE 4. Power Absorption in Cellular Compartments

Membranes	$PLD_{avg}(W/m^3)$ 6.78 MHz	$PLD_{avg}(W/m^3)$ 60 GHz
CP	0.33	32.04
N_i	0.23	31.72
N_{ims}	0.23	31.68
N_p	10.79	39.01
ER_L	0.19	30.29
GA_L	0.13	30.67
M_{ims}	0.48	33.62
M_L	0.11	29.34
V_L	0.15	31.48
EXM	0.48	32.68

of the charge concentration around N_m on both sides of the N_p (Fig. 3(b)). Additional simulations showed that the 2D approximation for the N_p underestimates $\boldsymbol{E}$ compared to the 3D N_p. $\boldsymbol{E}$ in the 2D N_p of a 1 µm nucleus was 50% (6.78 MHz) and 26.3% (60 GHz) lower than that of the 3D N_p. This is because physically the N_p provides a low resistance path for cellular currents to enter the nucleus and the 3D N_p constrains the currents and induced charges in the third dimension as well, thereby exhibiting higher $\boldsymbol{E}$. Thus, all molecular transport between N_i and CP is exposed to higher $\boldsymbol{E}$ and power compared to the rest of the cellular compartments.

From 10 MHz to 1 GHz, there is only a slight increment of the power loss in all cellular compartments. Above 5 GHz the power loss rises rapidly due to the increase in conductivity of the cellular compartments. The PLD_{avg} within N_p at 60 GHz was 1.2 times higher than that of the CP. Physically, the lower PLD_{avg} enhancement at 60 GHz compared to 6.78 MHz is due to the diminished resistance of the N_m and reduction in induced charges along its surface.

B. LOCAL ANALYSIS AT 6.78 MHz AND 60 GHz

1) EFFECT OF SIZE (ORGANELLES AND CELL)

Biological cells and organelles exhibit substantial natural diversity in size. Therefore, the power loss and E_{avg} in models of spherical cells and organelles with the radius ranging from 15 nm (size of exosome) to 98.5 µm (size of oocyte) [52] were computed using 2D axisymmetric approximation and analytical formulation reported in [53]. The numerical results were restricted to a radius of 15.3 µm due to computational limitations. The difference between analytical and numerical results was less than 0.43% for all possible combinations of the dielectric models. Therefore, in order to highlight the effect of size, the dielectric properties of CP and P_m were used for all sizes both in analytical calculations and numerical simulations.

Fig. 4(a) depicts the power loss as a function of the spherical model size at 6.78 MHz and 60 GHz. At 6.78 MHz, the results show that the power loss in a cell with the size of

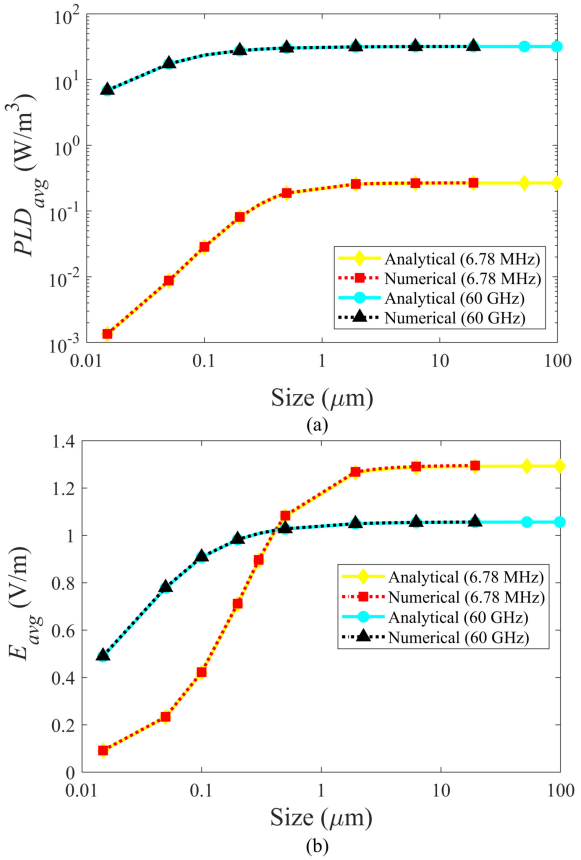

FIGURE 4. Effect of size of cells and organelles inside a spherical model: (a) PLD_{avg}; (b) E_{avg}.

an oocyte is roughly two hundred times higher than that of exosome for the same incident field. This is due to the fact that the charge density on the membrane decreases with size facilitating $\boldsymbol{E}$ penetration inside the cell or organelles (Fig. 4(b)). Note that the power loss and E_{avg} are almost independent of size above the radius of about 2 µm at 6.78 MHz. This is because larger structures require more time to charge completely. The aforementioned results suggest that the interior of smaller organelles such as V_L are better shielded from electromagnetic radiation than larger ones. At 60 GHz, when the radius increases from 15 nm to 98.5 µm, the power loss increases by roughly four times. This is because induced $\boldsymbol{E}$ is less dependent on membrane charging at 60 GHz as shown in Fig. 4(b). It is worthwhile to observe that E_{avg} almost does not depend on size above the radius of roughly 200 nm at 60 GHz. Fig. 4 shows a very good agreement between numerical results and analytical model.

2) EFFECT OF THE PRESENCE OF THE ORGANELLES

Power loss in vicinity of the organelles inside the cell exhibits a non-uniform distribution (Fig. 5). The power loss inside the CP with the organelles is 5.9% and 3.1% lower in comparison to the power loss in CP without the organelles at 6.78 MHz and 60 GHz, respectively. The decrease in power loss is due to the presence of low conductivity membranes within the cell. The weaker effect at 60 GHz is because the SC_m cause lower distortion of $\boldsymbol{E}$ as they do not have an adequate time to charge before the polarity of $\boldsymbol{E}$ switches. Contrarily, E_{avg} in CP with organelles is 19.4% and 2.75% higher than CP without organelles at 6.78 MHz and 60 GHz, respectively (Fig. 6). This increase is because each organelle within the cell acts as an electric dipole with induced charges across its interface.

Moreover, the power loss and $\boldsymbol{E}$ value are lower and confined to a smaller area for the organelles which are more streamlined in the direction of $\boldsymbol{E}$ (Fig. 5 and Fig. 6). For instance, M_{om} (M2) stores less charges because it is more streamlined and therefore exhibits the maximum power loss and $|E|$ in its proximity, which is 79.2% and 55.1% lower than that of mitochondria (M1) at 6.78 MHz. At 60 GHz, local variation of the power loss and $\boldsymbol{E}$ in the cell interior due to charging of organelles is less pronounced. In particular, the peak power loss and $|E|$ at 60 GHz in the vicinity of mitochondria (M2) is 45.6% and 25.8% lower than that of mitochondria (M1). The relatively weak effect at 60 GHz is due to the incomplete charging of M_{om}. Relatively high losses at the high curvature areas shown in Fig. 5 are due to the angular charge distribution induced by the applied field along the surface of the curved membrane. In other words, the local surface polarization charges depend on the curvature of the membrane's surface and the resulting local field is dipole in nature. Moreover, since the local curvatures within the cell are much smaller than the wavelength at both 6.78 MHz ($\approx 10^{-6}\lambda$) and 60 GHz ($\approx 10^{-3}\lambda$), the higher losses appear at high curvatures at both frequencies.

3) EFFECTS OF ORGANELLES POSITION

The distribution of the organelles within the cell also impacts the power loss and $\boldsymbol{E}$ in cytosol. For instance, the peak power loss and $|E|$ in the vicinity of mitochondria (M3) surrounded by two neighboring vesicles is 91.9% and 72.5% higher for the considered cell model than the background power loss and E_{avg} in CP at 6.78 MHz (Fig. 5(c) and Fig. 6(c)). This higher power loss is because the surface voltage gradient of the mitochondria produces $\boldsymbol{E}$ which superimposes positively with $\boldsymbol{E}$ of neighboring vesicles at this location. Similarly, due to a smaller gap between mitochondria (M3) and adjacent vesicles at 60 GHz, the maximum power loss and $|E|$ are 53.1% and 31.6% higher than the background power loss and E_{avg} in CP (Fig. 5(h) and Fig. 6(h)).

Power loss and $\boldsymbol{E}$ in the organelles located close to other larger organelles is also higher than those near smaller ones. For instance, the mitochondria (M4) positioned just below the nucleus exhibits 45% higher power loss and 25% higher E_{avg} in M_{om} than that induced in mitochondria (M1) at 6.78 MHz (Fig. 5(a) and Fig. 6(a)). This is because the larger surface of a membrane bound structure stores more charge than a smaller structure resulting in higher distortion of $\boldsymbol{E}$. In other words, the charging of smaller organelles has weakened effect because the region of impact of small organelles is small and

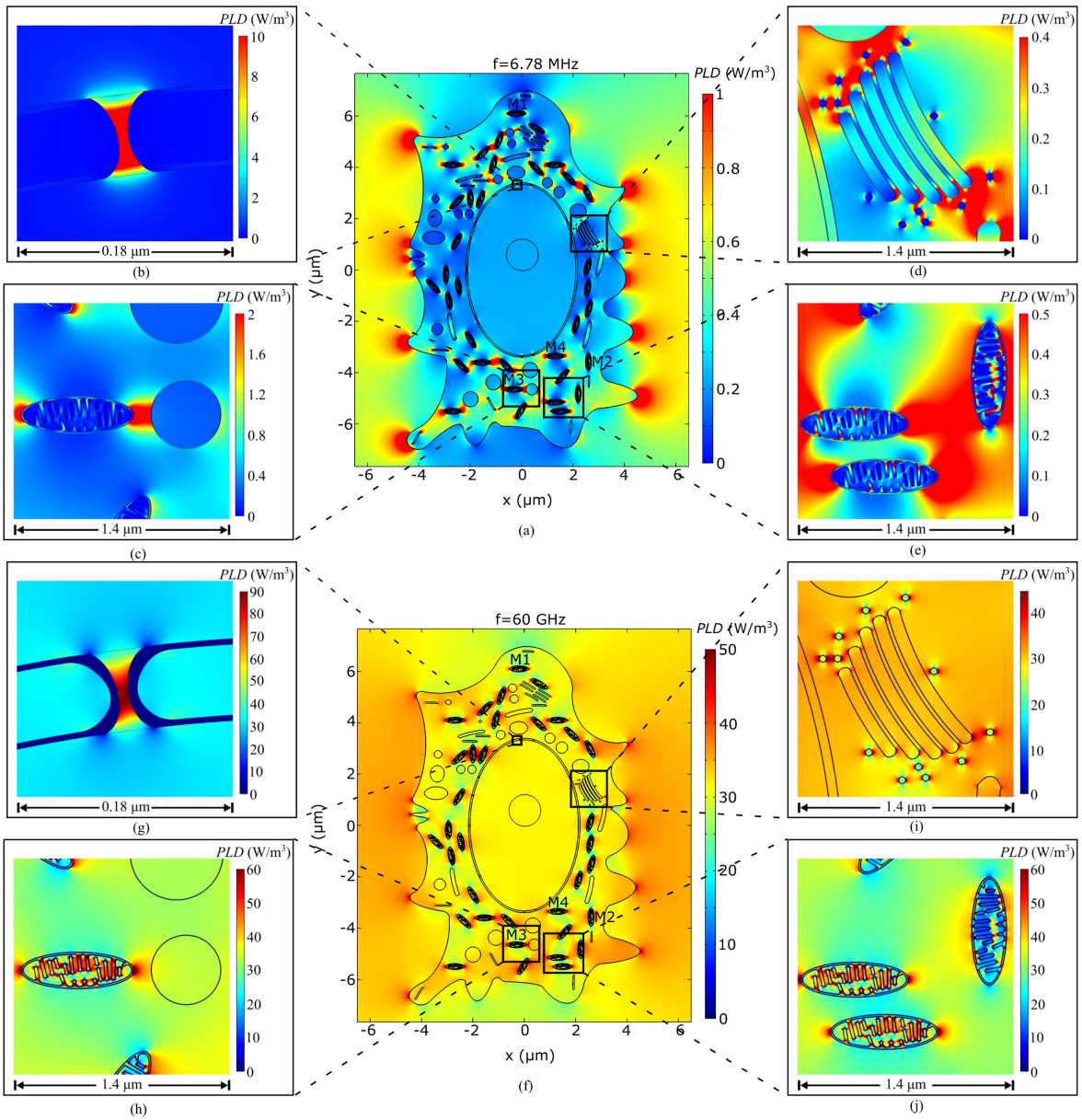

FIGURE 5. ***PLD*** **distribution: (a), (f) cell; (b), (g) nuclear pore; (c), (h) vesicle; (d), (i) Golgi apparatus; (e), (j) mitochondria.**

not sufficient to modify nearby oscillators. A similar trend is observable at 60 GHz. The power loss and E_{avg} in M_{om} of mitochondria (M4) is 5.55% and 3.05% higher than that of mitochondria (M1) (Fig. 5(f) and 6(f)).

4) EFFECT OF ORGANELLES ORIENTATION

The power loss and $\boldsymbol{E}$ are sensitive to the orientation of applied $\boldsymbol{E}$ with respect to the major or minor axis of the mitochondria. In case of alignment of $\boldsymbol{E}$ with the minor axis of the mitochondria at 6.78 MHz, the power loss and E_{avg} in the M_{om} are 82.3% and 62.8% higher than the case when $\boldsymbol{E}$ is aligned with the major axis of mitochondria (Fig. 5(e) and 6(e)). The higher power loss in the former case is because the flat portion of M_{om} is perpendicular to the incident $\boldsymbol{E}$ thereby inducing higher $\boldsymbol{E}$. Likewise, at 60 GHz when $\boldsymbol{E}$ is parallel to the minor axis of the mitochondria, the power loss and E_{avg} in the M_{om} are 81.9% and 59.5% higher than the case when $\boldsymbol{E}$ is parallel to the major axis of the mitochondria (Fig. 5(j) and 6(j)).

On the opposite, the power loss and E_{avg} in the lumen of mitochondria whose major axis is aligned with $\boldsymbol{E}$ are 33.75% and 7.65% higher than that mitochondria whose minor axis is aligned with $\boldsymbol{E}$ at 6.78 MHz (Fig. 5(e) and 6(e)). In contrast, at 60 GHz, when $\boldsymbol{E}$ is parallel to the minor axis of mitochondria, the power loss and E_{avg} inside its lumen are 42.1% and 25.2% higher than when $\boldsymbol{E}$ is parallel to major axis (Fig. 5(j) and 6(j)). The lower power loss and E_{avg} in the latter case are because of diminished charging of M_{im} at 60 GHz. The results indicate that only a subpopulation of the organelles with the

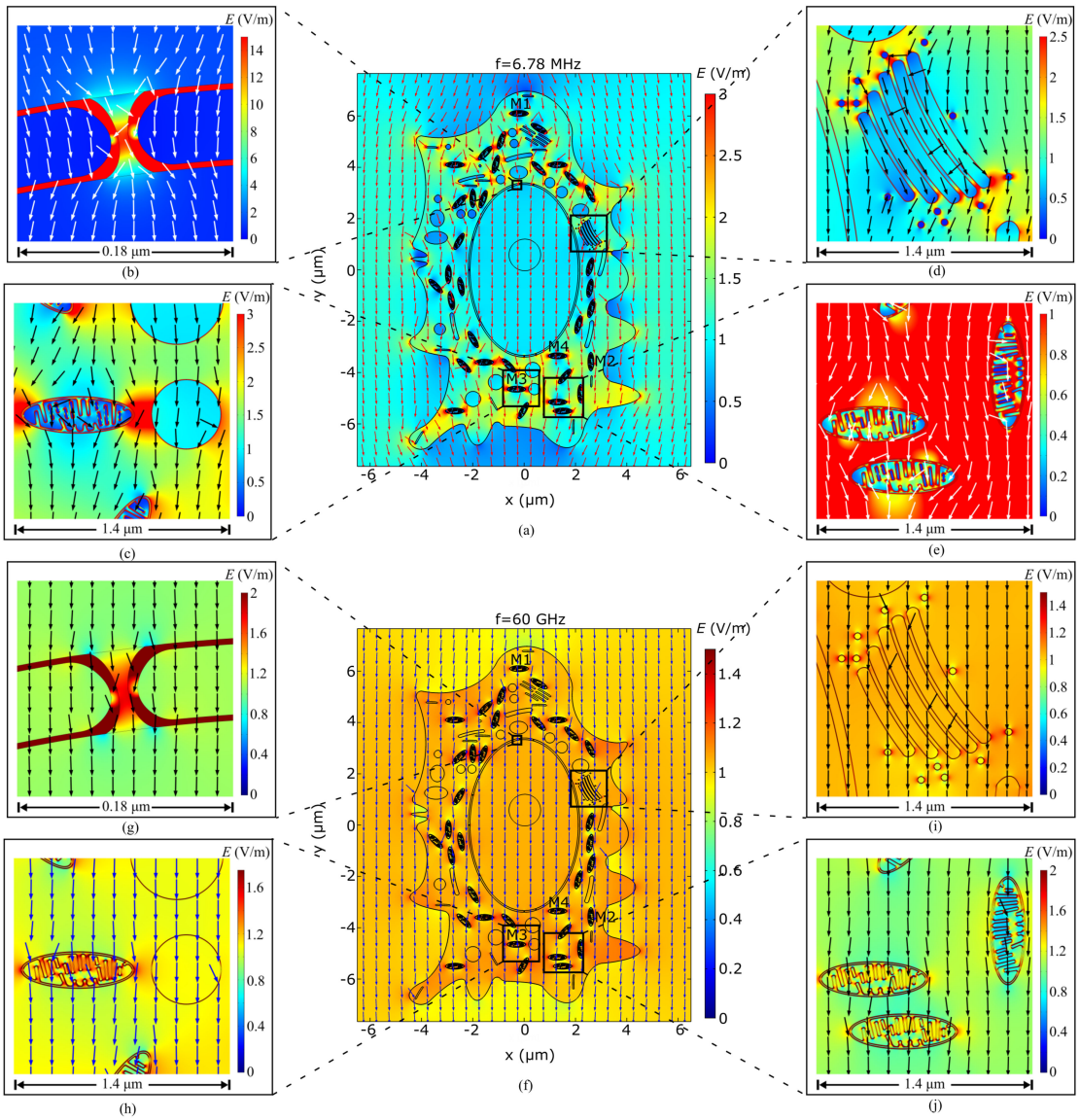

FIGURE 6. ***E*** **distribution: (a), (f) cell; (b), (g) nuclear pore; (c), (h) vesicle; (d), (i) Golgi apparatus; (e), (j) mitochondria.**

minimum streamlinedness and largest height in the direction of the ***E*** are excited to produce the maximum power loss.

5) RELEVANCE FOR FUTURE INVESTIGATION ON BIOLOGICAL EFFECTS

Potential biological consequences and impact of aforementioned variations in the power loss and ***E*** on cell function have not been investigated so far. From a biological point of view, the higher power loss observed in the N_p (Fig. 5(b) and 5(g)), V_L (Fig. 5(d) and 5(g)), and GA_L (Fig. 5(c) and 5(h)) suggests that priority can be given to investigate the effect of the exposure on intracellular traffic. The power absorption at the level of the cristae and M_{im} highlights the hypothesis of a potential interference with the respiratory chain and possible production of reactive oxygen species. Further biological investigations of these aspects are out of the scope of this study and constitute one of its perspectives.

IV. CONCLUSION

This paper presents, for the first time, the microdosimetric analysis of a keratinocyte at frequencies upcoming for mmWave 5 G/6 G and wireless power transfer systems. The results quantitatively show dispersive absorption in the cell model. In particular, the average power loss within all its interior compartments at 6.78 MHz (0.21 W/m^3) and 60 GHz (31.4 W/m^3) was 35.7% and 1.95% lower than that of the cytoplasm (CP) (0.33 W/m^3 at 6.78 MHz and 32.04 W/m^3 at 60 GHz) due to the frequency-dependent shielding effect of membranes. In other words, in average more than 51.8% and 98.9% of the incident field reaches cellular compartments at 6.78 MHz and 60 GHz, respectively. Thus, the mmWave

exhibit higher capability to cause potential microthermal effects at subcellular level than HF band. Additionally, average electric field (E_{avg}) inside nuclear pores (N_p) was roughly 5 times (4.96 V/m at 6.78 MHz) and 1.1 times (1.1 V/m at 60 GHz) higher than the incident field while the average power loss was 32.7 times (10.8 W/m^3 at 6.78 MHz) and 1.2 times (39.01 W/m^3 at 60 GHz) higher than that of CP. Furthermore, induced E in 3D N_p was 50% (6.78 MHz) and 26.3% (60 GHz) higher than the 2D N_p. This suggests that any narrow regions between membrane bound structures within the cell will exhibit higher power loss compared to surrounding cytoplasm due to induced surface charges along the membranes. The average power loss within the large cell is roughly 200 times and 4 times higher than that in a small vesicle (exosome) at 6.78 MHz and 60 GHz, respectively. Thus, the interior of smaller organelles, such as vesicles, are better shielded from non-ionizing radiation compared to larger ones. Finally, in case of electric field parallel to the minor axis of the mitochondria, the power loss and E_{avg} in the outer mitochondria membrane (M_{om}) are higher (82.3% and 62.8% at 6.78 MHz, 81.9% and 59.5% at 60 GHz) compared to the case when it is parallel to the major axis of mitochondria. Consequently, the maximum absorption within the subcellular membranes takes place when electric field is perpendicular to the longest dimension of the organelles. This study provides valuable electromagnetic dosimetry data regarding non-uniform micro-scale power deposition in cells.

The electric field measurements with high spatial resolution would be required for experimental validation of the numerical results. Despite the excellent sensitivity, the conventional methods for recording membrane potential (microelectrodes and voltage-sensitive dyes) [54] and mapping intracellular electric field (nanoparticles) [55] only provide a glimpse of the total electric field profile within the cell. Similarly, the infrared thermography suffers from insufficient spatial resolution (≈10 μm) [56]. Development of reliable methods for precise measurement of local subcellular electric field and temperature constitutes one of the perspectives of this work.

REFERENCES

[1] *Cisco Visual Networking Index: Global Mobile Data Traffic Forecast Update*, 2017-2022, Feb. 2019. [Online]. Available: https://davidellis.ca/wp-content/uploads/2019/12/cisco-vni-mobile-data-traffic-feb-2019.pdf.

[2] L. Chettri and R. Bera, "A comprehensive survey on Internet of Things (IoT) toward 5G wireless systems," *IEEE Internet Things J.*, vol. 7, no. 1, pp. 16–32, Jan. 2020.

[3] *IEEE Standard for WirelessMAN-Advanced Air Interface for Broadband Wireless Access Systems*, IEEE Standard 802.16.1, 2012.

[4] "ISO/IEC/IEEE International Standard for Information technology–Telecommunications and information exchange between systems–Local and metropolitan area networks–Specific requirements-Part 11: Wireless LAN Medium Access Control (MAC) and Physical Layer (PHY) Specifications Amendment 3: Enhancements for Very High Throughput in the 60 GHz Band (adoption of IEEE Std 802.11ad-2012)," in *ISO/IEC/IEEE 8802-11:2012/Amd.3:2014(E)*, pp. 1–634, Mar. 2014, doi: 10.1109/IEEESTD.2014.6774849.

[5] "IEEE Standard for Information technology–Local and metropolitan area networks–Specific requirements–Part 15.3: Amendment 2: Millimeter-wave-based Alternative Physical Layer Extension," in *IEEE Std 802.15.3c-2009 (Amendment to IEEE Std 802.15.3-2003)*, pp. 1–200, Oct. 2009, doi: 10.1109/IEEESTD.2009.5284444.

[6] *Fact Sheet: Spectrum Frontiers Rules Identify, Open up Vast Amounts of New High-Band Spectrum for Next Generation (5G) Wireless Broadband*. Accessed: Jul. 14, 2016. [Online]. Available: https://www.fcc.gov/document/rules-facilitate-next-generation wireless technologies.

[7] M. G. Bautista, H. Zhu, X. Zhu, Y. Yang, Y. Sun, and E. Dutkiewicz, "Compact millimeter-wave bandpass filters using quasi-lumped elements in 0.13- m (Bi)-CMOS technology for 5G wireless systems," *IEEE Trans. Microw. Theory Techn.*, vol. 67, no. 7, pp. 3064–3073, Jul. 2019.

[8] J. Lawson, D. C. Yates, and P. D. Mitcheson, "High Q-coil measurement for inductive power transfer," *IEEE Trans. Microw. Theory Techn.*, vol. 67, no. 5, pp. 1962–1973, May 2019.

[9] G. Pucihar, T. Kotnik, B. Valič, and D. Miklavčič, "Numerical determination of transmembrane voltage induced on irregularly shaped cells," *Ann. Biomed. Eng.*, vol. 34, no. 4, pp. 642–652, Apr. 2006.

[10] T. Kotnik and D. Miklavcic, "Second-order model of membrane electric field induced by alternating external electric fields," *IEEE Trans. Biomed. Eng.*, vol. 47, no. 8, pp. 1074–1081, Aug. 2000.

[11] T. Kotnik and D. Miklavčič, "Analytical description of transmembrane voltage induced by electric fields on spheroidal cells," *Biophys. J.*, vol. 79, no. 2, pp. 670–679, Aug. 2000.

[12] J. Gimsa and D. Wachner, "Analytical description of the transmembrane voltage induced on arbitrarily oriented ellipsoidal and cylindrical cells," *Biophys. J.*, vol. 81, no. 4, pp. 1888–1896, Oct. 2001.

[13] L.-M. Liu and S. F. Cleary, "Absorbed energy distribution from radiofrequency electromagnetic radiation in a mammalian cell model: Effect of membrane-bound water," *Bioelectromagnetics*, vol. 16, no. 3, pp. 160–171, 1995.

[14] C. Merla *et al.*, "Novel passive element circuits for microdosimetry of nanosecond pulsed electric fields," *IEEE Trans. Biomed. Eng.*, vol. 59, no. 8, pp. 2302–2311, Aug. 2012.

[15] R. P. Joshi, Q. Hu, and K. H. Schoenbach, "Modeling studies of cell response to ultrashort, high-intensity electric fields-implications for intracellular manipulation," *IEEE Trans. Plasma Sci.*, vol. 32, no. 4, pp. 1677–1686, Aug. 2004.

[16] K. C. Smith, T. R. Gowrishankar, A. T. Esser, D. A. Stewart, and J. C. Weaver, "The spatially distributed dynamic transmembrane voltage of cells and organelles due to 10 ns pulses: Meshed transport networks," *IEEE Trans. Plasma Sci.*, vol. 34, no. 4, pp. 1394–1404, Aug. 2006.

[17] T. R. Gowrishankar, A. T. Esser, Z. Vasilkoski, K. C. Smith, and J. C. Weaver, "Microdosimetry for conventional and supra-electroporation in cells with organelles," *Biochem. Biophys. Res. Commun.*, vol. 341, no. 4, pp. 1266–1276, Mar. 2006.

[18] M. Liberti, F. Apollonio, C. Merla, and G. d'Inzeo, "Microdosimetry in the microwave range: A quantitative assessment at single cell level," *IEEE Antennas Wireless Propag. Lett.*, vol. 8, pp. 865–868, 2009.

[19] G. Pucihar, D. Miklavcic, and T. Kotnik, "A time-dependent numerical model of transmembrane voltage inducement and electroporation of irregularly shaped cells," *IEEE Trans. Biomed. Eng.*, vol. 56, no. 5, pp. 1491–1501, May 2009.

[20] C. Merla, M. Liberti, F. Apollonio, C. Nervi, and G. d'Inzeo, "A 3-D microdosimetric study on blood cells: A permittivity model of cell membrane and stochastic electromagnetic analysis," *IEEE Trans. Microw. Theory Techn.*, vol. 58, no. 3, pp. 691–698, Mar. 2010.

[21] J. Dermol-Cerne and D. Miklavcic, "From cell to tissue properties-modeling skin electroporation with pore and local transport region formation," *IEEE Trans. Biomed. Eng.*, vol. 65, no. 2, pp. 458–468, Feb. 2018.

[22] A. Denzi *et al.*, "Microdosimetric study for nanosecond pulsed electric fields on a cell circuit model with nucleus," *J. Membr. Biol.*, vol. 246, no. 10, pp. 761–767, Oct. 2013.

[23] A. Denzi, H. Hanna, F. M. Andre, L. M. Mir, F. Apollonio, and M. Liberti, "Microdosimetry for pulsed E fields in a realistic models of cells and endoplasmic reticulum," in *Proc. 14th Int. Conf. Synthesis, Modeling, Anal. Simul. Methods Appl. Circuit Des.*, Giardini Naxos, Italy, 2017, pp. 1–3.

[24] A. D. Angelis *et al.*, "Confocal microscopy improves 3D microdosimetry applied to nanoporation experiments targeting endoplasmic reticulum," *Front. Bioeng. Biotechnol.*, vol. 8, pp. 1–9, 2020.

[25] H. Qiu, S. Xiao, and R. P. Joshi, "Simulations of voltage transients across intracellular mitochondrial membranes due to nanosecond electrical pulses," *IEEE Trans. Plasma Sci.*, vol. 42, no. 10, pp. 3113–3120, Oct. 2014.
[26] L. Retelj, G. Pucihar, and D. Miklavcic, "Electroporation of intracellular liposomes using nanosecond electric pulses-a theoretical study," *IEEE Trans. Biomed. Eng.*, vol. 60, no. 9, pp. 2624–2635, Sep. 2013.
[27] H. Hanna, A. Denzi, M. Liberti, F. M. André, and L. M. Mir, "Electropermeabilization of inner and outer cell membranes with microsecond pulsed electric fields: Quantitative study with calcium ions," *Sci. Rep.*, vol. 7, no. 1, Dec. 2017, Art. no. 13079.
[28] T.-T. Sun and H. Green, "Differentiation of the epidermal keratinocyte in cell culture: Formation of the cornified envelope," *Cell*, vol. 9, no. 4, pp. 511–521, Dec. 1976.
[29] W. Montagna and P. F. Parakkal, "The epidermis," in *Structure Function Skin*, 3rd ed. New York, NY, USA: Academic, 1974, pp. 18–74.
[30] A. J. P. Klein-Szanto, "Stereological baseline data of normal human epidermis," *J. Invest. Dermatol.*, vol. 68, no. 2, pp. 73–78, Feb. 1977.
[31] A. S. Zelickson and J. F. Hartmann, "An electron microscopic study of human epidermis," *J. Invest. Dermatol.*, vol. 36, no. 2, pp. 65–72, Feb. 1961.
[32] N. Panté and B. Fahrenkrog, "Exploring nuclear pore complex molecular architecture by immuno-electron microscopy using xenopus oocytes," *Methods Cell Biol.*, vol. 122, pp. 81–98, 2014.
[33] A. C. Guyton and J. E. Hall, Eds., *Textbook of Medical Physiology*, 11th ed. Philadelphia, PA, USA: Saunders, 2006, pp. 11–26.
[34] D. J. Morré and H. H. Mollenhauer, "Structure," in *The Golgi Apparatus: The First 100 Years*. New York, NY, USA: Springer, 2009, pp. 9–38.
[35] R. S. Polishchuk and A. A. Mironov, "Structural aspects of golgi function," *Cell. Mol. Life Sci.*, vol. 61, no. 2, pp. 146–158, Jan. 2004.
[36] T. G. Frey and C. A. Mannella, "The internal structure of mitochondria," *Trends Biochem. Sci.*, vol. 25, no. 7, pp. 319–324, Jul. 2000.
[37] M. H. Ross and W. Pawlina, *Histology: A. Text and Atlas: With Correlated Cell and Molecular Biology*, 7th ed. Philadelphia, PA, USA: Lippincott Williams & Wilkins, 2016, pp. 52–82.
[38] M. Terasaki *et al.*, "Stacked endoplasmic reticulum sheets are connected by helicoidal membrane motifs," *Cell*, vol. 154, no. 2, pp. 285–296, Jul. 2013.
[39] C. C. Selby, "An electron microscope study of the epidermis of mammalian skin in thin sections I. Dermo-epidermal junction and basal cell layer," *J. Biophys. Biochem. Cytol.*, vol. 1, no. 5, pp. 429–444, Sep. 1955.
[40] C. Merla, M. Liberti, F. Apollonio, and G. d'Inzeo, "Quantitative assessment of dielectric parameters for membrane lipid bi-layers from RF permittivity measurements," *Bioelectromagnetics*, vol. 30, no. 4, pp. 286–298, May 2009.
[41] M. Casciola, M. Liberti, A. Denzi, A. Paffi, C. Merla, and F. Apollonio, "A computational design of a versatile microchamber for in vitro nanosecond pulsed electric fields experiments," *Integration*, vol. 58, pp. 446–453, Jun. 2017.
[42] T. Kotnik and D. Miklavcic, "Theoretical evaluation of the distributed power dissipation in biological cells exposed to electric fields," *Bioelectromagnetics*, vol. 21, pp. 385–394, Jul. 2000.
[43] Denzi *et al.*, "Assessment of cytoplasm conductivity by nanosecond pulsed electric fields," *IEEE Trans. Biomed. Eng.*, vol. 62, no. 6, pp. 1595–1603, Jun. 2015.
[44] B. Alberts, A. Johnson, J. Lewis, M. Raff, K. Roberts, and P. Walter, *Molecular Biology of the Cell*, 6th ed. New York, NY, USA: Taylor & Francis, 2002, pp. 641–694.
[45] P. L. Paine, L. C. Moore, and S. B. Horowitz, "Nuclear envelope permeability," *Nature*, vol. 254, pp. 109–114, 1975.
[46] J. D. Jackson, *Classical Electrodynamics*, 3rd ed. New York, NY, USA: Wiley, 1999, pp. 237–294.
[47] International Commission on Non-Ionizing Radiation Protection (ICNIRP), "Guidelines for limiting exposure to electromagnetic fields (100 kHz to 300 GHz)," *Health Phys.*, vol. 118, no. 5, pp. 483–524, May 2020.
[48] S. Gabriel, R. W. Lau, and C. Gabriel, "The dielectric properties of biological tissues: III. Parametric models for the dielectric spectrum of tissues," *Phys. Med. Biol.*, vol. 41, no. 11, pp. 2271–2293, Nov. 1996.
[49] Y. Mi, J. Xu, C. Yao, and H. Liu, "Electroporation modeling of a single cell exposed to high-frequency nanosecond pulse bursts," *IEEE Trans. Dielectr. Electr. Insul.*, vol. 26, no. 2, pp. 461–468, Apr. 2019.
[50] M. Zhadobov, S. I. Alekseev, Y. Le Dréan, R. Sauleau, and E. E. Fesenko, "Millimeter waves as a source of selective heating of skin," *Bioelectromagnetics*, vol. 36, no. 6, pp. 464–475, Jul. 2015.
[51] H. L. Gerber, R. P. Joshi, and C. C. Tseng. "Using bode plots to access intracellular coupling," *IEEE Trans. Plasma Sci.*, vol. 36, no. 4, pp. 1659–1664, Aug. 2008.
[52] R. Milo and R. Phillips, "Size and geometry," in *Cell Biology by the Numbers*. New York, NY, USA: Garland Science, Taylor & Francis Group, 2016, pp. 3–63.
[53] A. G. Pakhomov, D. Miklavcic, and M. M. Markov, *Advanced Electroporation Techniques in Biology and Medicine*. Boca Raton, FL, USA: CRC Press, 2010, pp. 51–70.
[54] P. Liu and E. W. Miller, "Electrophysiology, unplugged: Imaging membrane potential with fluorescent indicators," *Accounts Chem. Res.*, vol. 53, no. 1, pp. 11–19, Dec. 2019.
[55] K. M. Tyner, R. Kopelman, and M. A. Philbert, "'Nanosized voltmeter' enables cellular-wide electric field mapping," *Biophy. J.*, vol. 93, no. 4, pp. 1163–1174, Aug. 2007.
[56] T. Bai, and N. Gu, "Micro/nanoscale thermometry for cellular thermal sensing," *Small*, vol. 12, no. 34, pp. 4590–4610, Sep. 2016.

ZAIN HAIDER received the M.S. degree in electrical engineering from the National University of Sciences and Technology, Islamabad, Pakistan, in 2017. He is currently working toward the Ph.D. degree in bioelectromagnetics with the Institute of Electronics and Telecommunications of Rennes (IETR), University of Rennes 1, Rennes, France. His research interests include microdosimetry and metamaterials.

DENYS NIKOLAYEV (Member, IEEE) received the M.S. degree (*summa cum laude*) in electronics and telecommunications from Lviv Polytechnic National University, Ukraine, in 2008, and the joint Ph.D. degrees in electronics from the Institute of Electronics and Telecommunication of Rennes, Rennes, France, and in electrical engineering from the University of West Bohemia, Pilsen, Czechia, in 2017.

He was a Postdoctoral Fellow with Imec/Ghent University, Belgium, until 2018, a Scientist with École polytechnique fédérale de Lausanne, Lausanne, Switzerland, until 2020, and then joined the French National Center for Scientific Research, Paris, France, as a Permanent Researcher. He has authored one book chapter, 20 journal papers, 34 publications in international conference proceedings, and holds four patents. His research interests include wireless bioelectronics and biosensors, antenna theory and design for body-centric networks, bioelectromagnetics, and numerical methods in electromagnetics.

Dr. Nikolayev was the recipient of the Best Ph.D. Dissertation Award by the Foundation Rennes One, the Young Scientist Award at the International Conference EMBEC/NBC 2017, the Best Paper Award at the URSI-France 2017 Workshop, and the Poster Award at BioEM 2015. He was a laureate of the Eiffel Excellence Doctoral Grant (2015/2016).

YVES LE DRÉAN was born in 1964. He received the Ph.D. degree and Habilitation á Diriger des Recherches degree in biology from the Université de Rennes 1, Rennes, France, in 1993 and 2007, respectively. In 1994, he joined the Hospital for Sick Children, Toronto, ON, Canada, as a Postdoctoral Fellow. Since 1997, he has been an Associate Professor with the Université de Rennes 1, where he teaches molecular biology and biochemistry. He has authored or coauthored two book chapters, 35 journal publications, and 55 communications in national and international conferences. His main subject of interest focuses on the control of genetic expression. His current research activity focuses on the investigations of cell responses to environmental stress. Since 2004, he has been also actively involved in the field of biological effects of electromagnetic waves.

ANNALISA DE ANGELIS (Member, IEEE) received the M.S. degree in biomedical engineering from the University of Rome "Sapienza," Rome, Italy, in 2009, and the Ph.D. degree in "high frequencies electronics, photonics, and systems" from the Vincent Couderc's Group, Xlim Research Institute, University of Limoges, Limoges, France, in 2012. During the academic period, she collaborated with emergent researchers in the field of bioelectromagnetics, carrying out interesting studies on electro-induced cell membrane permeabilization detection using nonlinear optical approaches (stimulated Raman spectroscopy). Since 2014, she has been a Postdoctoral Fellow with the De Luca's Lab, Institute of Protein Biochemistry, National Research Council of Italy, Naples, Italy. Her main research interests include linear and nonlinear Raman spectroscopy and imaging, and optoelectronic devices development for biological applications.

MICAELA LIBERTI (Member, IEEE) received the Laurea and Ph.D. degrees in electronic engineering from Sapienza, University of Rome, Italy, in 1995 and 2000, respectively. From 2001 to 2002, she was a Postdoctoral Fellow with the Italian Inter-University Center of Electromagnetic Fields and Biosystems (ICEmB). In 2002, she became an Assistant Professor with the Department of Electronic Engineering, University of Rome "La Sapienza." Since 2008, she has been a member of the Scientific Council of the European Bioelectromagnetic Association (EBEA). In 2011, she acted as the General Chair of EBEA2011, she is in COST TD1104: European network for development of electroporation-based technologies and treatments. Her scientific research interests include interaction mechanisms between EM fields and biological systems, dosimetric evaluations at the microscopic level, exposure systems dosimetry, and design.

RONAN SAULEAU (Fellow, IEEE) graduated in electrical engineering and radio communications from the Institut National des Sciences Appliqués, Rennes, France, in 1995, and received the Agrégation degree from the Ecole Normale Supérieure de Cachan, France, in 1996, and the Doctoral degree in signal processing and telecommunications and the Habilitation á Diriger des Recherches degree from the University of Rennes1, Rennes, France, in 1999 and 2005, respectively.

From September 2000 to November 2005, and from December 2005 to October 2009, he was an Assistant Professor and Associate Professor with the University of Rennes 1, where, since 2009, he has been a Full Professor. He has shared the responsibility of the research activity focuses on antennas at IETR in 2010 and 2011. He was the Co-Director of the Research Department Antenna and Microwave Devices, IETR, and the Deputy Director with IETR from 2012 to 2016. He is currently the Director of IETR. He was involved in more than 60 research projects at the national and European levels and was Co-Supervised 23 Postdoctoral Fellows, 44 Ph.D. students, and 50 master's students. He has received 17 patents, and authored or coauthored more than 250 journal papers and 510 publications in international conferences and workshops. His current research interests include numerical modeling (mainly FDTD), millimeter-wave printed and reconfigurable (MEMS) antennas, substrate integrated waveguide antennas, lens-based focusing devices, periodic and nonperiodic structures (electromagnetic bandgap materials, metamaterials, reflectarrays, and transmitarrays), and biological effects of millimeter waves.

Prof. Sauleau was the recipient of the 2004 ISAP Conference Young Researcher Scientist Fellowship, Japan, and the first Young Researcher Prize in Brittany, France, in 2001 for his research work on gain-enhanced Fabry-Perot antennas. In September 2007, he was elevated to Junior Member of the Institut Universitaire de France. He was Awarded the Bronze Medal by CNRS in 2008 and the Silver Medal in 2020. He was the co-recipient of several international conference awards with some of his students (BioEM2005, BEMS'2006, MRRS'2008, E-MRS'2011, BEMS'2011, IMS'2012, Antem'2012, BioEM'2015, and EuCAP'2019). He was the Guest Editor of the IEEE TRANSACTIONS ON ANTENNAS AND PROPAGATION Special Issue on Antennas and Propagation at mm and sub mm Waves. He was the National Delegate for several EU COST actions. He was the National Delegate for EurAAP and a Member on the Board of Director of EurAAP from 2013 to 2018.

MAXIM ZHADOBOV (Senior Member, IEEE) received the M.S. degree in electromagnetics from the University of Nizhny Novgorod, Nizhny Novgorod, Russia, in 2003, and the Ph.D. and Habilitation á Diriger des Recherches degrees from the Institut d'Electronique et des Technologies du numerique (IETR), University of Rennes 1, Rennes, France, in 2006 and 2016, respectively.

He was a Postdoctoral Researcher with the Center for Biomedical Physics, Temple University, Philadelphia, PA, USA, until 2008, and then joined the French National Center for Scientific Research (CNRS).

He is currently the Principal Investigator of biomedical electromagnetics with the IETR/CNRS and the Head of the WAVES Research Team, IETR. He has coauthored five book chapters, five patents, more than 75 research papers in peer-reviewed international journals, and 180 contributions to conferences and workshops. His research interests include innovative biomedical applications of electromagnetic fields and associated technologies. His review article in the *International Journal of Microwave and Wireless Technologies* was the most cited paper in 2016–2020. A paper authored or coauthored by his research group in 2019 is in journal Top 100 of Nature Scientific Reports. He was involved in 24 research projects (12 as PI).

Dr. Zhadobov was the TPC Co-Chair of BioEM 2021 and BioEM 2020. He was a TPC Member and/or Session Organizer with international conferences, including BioEM 2019, EuMW 2019, IEEE iWEM 2017, MobiHealth 2015-2017, BodyNets 2016, and IMWS-Bio 2014. He is an elected Member of EBEA Council, Member of IEEE TC95.4, and the Vice-President of URSI France Commission K. He is an Associate Editor of IEEE JOURNAL OF ELECTROMAGNETICS, RF AND MICROWAVES IN MEDICINE AND BIOLOGY and was the Guest Editor of several special issues, including Human Exposure in 5G and 6G Scenarios of Applied Sciences and Advanced Electromagnetic Biosensors for Medical, Environmental and Industrial Applications of Sensors. He was also on review boards of more than 15 international journals and conferences, and was acting as an expert at research councils worldwide. He was the recipient of the CNRS Medal in 2018, the EBEA Award for Excellence in Bioelectromagnetics in 2015, and Brittany's Young Scientist Award in 2010. Since 2010, his Ph.D. students have been recipients of seven national scientific awards and five awards from the Bioelectromagnetics Society, URSI, and the IEEE Antennas and Propagation Society.